Int J Adv Manuf Technol (2013) 67:2157–2169
DOI 10.1007/s00170-012-4637-7

ORIGINAL ARTICLE

Butt autogenous laser welding of AA 2024 aluminium alloy thin sheets with a Yb:YAG disk laser

Fabrizia Caiazzo · Vittorio Alfieri ·
Francesco Cardaropoli · Vincenzo Sergi

Received: 24 May 2012 / Accepted: 8 November 2012

Abstract Higher productivity, lower distortion and better penetration are the main advantages provided by laser welding in comparison with conventional processes. A Trumpf TruDisk 2002 Yb:YAG disk laser is used in this work to increases productivity and quality. Aluminium alloys lead to many technological issues in laser welding, resulting in shallow penetration and defects. In particular, AA 2024 aluminium alloy in a thin sheet is investigated in this paper, being it is used extensively in the automotive and aerospace industries. Bead-on-plate and butt autogenous laser welding tests with continuous wave emission on 1.25 mm thick AA 2024 aluminium alloy sheets were examined morphologically and micro-structurally. The geometric and mechanical features of the welding bead were evaluated via a three-level experimental plan. In addition to the power and speed which are traditionally referred to, beam defocusing was considered as an additional governing factor in a central composite design scheme because it massively affects keyhole conditions. Softening in the fused zone is discussed via Vickers microhardness testing and magnesium loss through energy dispersive spectrometry. After properly performing the modelling and optimisation of the fused zone and the cross-section shape factor as the response variables, the laser welding conditions for thin sheets of AA 2024 aluminium alloy are suggested. X-ray and tensile tests were conducted on the specimens obtained with the recommended processing parameters to characterise the AA 2024 disk laser welded beads.

Keywords Laser welding · Aluminium alloy · AA 2024 · Disk laser · Defocusing · Optimisation

1 Introduction

Among all of the commercial high-strength heat-treatable and age-hardenable aluminium alloys, AA 2024 was among the first ones to be used and is still one of the most common. Belonging to group 2xxx, its major alloying element is copper; the complete chemical composition is given in Table 1. Although its tensile strength, its Young modulus and its hardness are much lower than those of steel, its excellent plasticity, corrosion resistance, electric conductivity and strength to weight ratio make it particularly useful in a wide range of applications and manufacturing areas, especially in the automotive, military and aerospace industries, because weight reduction is one of the most effective ways to enhance efficiency in vehicles and aircraft [1–3]. In particular, interest has been shown in studying welding of AA 2024 thin sheets that are under 2 mm in thickness and satisfactory results have been achieved using Nd:YAG and CO_2 lasers sources [3].

Aluminium and its alloys can be joined by as many or more methods than any other metal, such as gas arc welding, resistance welding, friction welding, stud welding, electron and laser beam welding. Despite these advantages, the applications of aluminium are usually restricted because several challenges are involved in the welding processes due to oxidation, cracking, softening and the solubility of hydrogen in the molten metal, which results in porosity within the welding bead [4–6]. Moreover, the thermal expansion of aluminium is approximately twice that of steel; in

F. Caiazzo (✉) · V. Alfieri · F. Cardaropoli · V. Sergi
Dip. di Ingegneria Industriale, Università degli Studi di Salerno,
84084 Fisciano, Italy
e-mail: f.caiazzo@unisa.it

V. Alfieri
e-mail: valfieri@unisa.it

F. Cardaropoli
e-mail: fcardaro@unisa.it

V. Sergi
e-mail: sergi@unisa.it

Table 1 Nominal chemical composition of AA 2024 (weight percent)

Cu	Mg	Mn	Si	Fe	Cr	Zn	Ti	Al
3.80÷4.90	1.20÷1.80	0.30÷0.90	0.50	0.50	0.1	0.25	0.15	Bal.

particular, aluminium welding beads shrink approximately 6 % by volume during solidification [4].

Research has been already performed to understand the behaviour of AA 2024 in TIG welding and friction stir welding (FSW). The high heat inputs in TIG welding produce a large heat-affected zone (HAZ), where softening and hot cracking are observed [7], while the metal is not melted in FSW, thus resulting in less micro-structural changes with a partial local recovery in strength due to the high shear stresses induced by the tool motion [6]; nevertheless, a counterproductive reduction in the corrosion resistance has been noticed [8] and very slow welding rates are required.

The benefits of laser welding have been clearly demonstrated [9–11], and thus recent studies have considered the welding of AA 2024 using different laser sources [1, 3, 5, 12, 13]. Deeper penetration as a consequence of metal vaporisation in keyhole welding conditions, lower distortion, narrow HAZ and higher productivity are obtained compared to conventional welding process due to the localised heat input [14, 15]. However, laser welding is still a great challenge because it involves several physical and chemical processes. In addition to any typical issues in aluminium welding, a detailed understanding of the phenomena of laser welding is further complicated by material features, such as high thermal conductivity and low absorptance. Although the melting temperature of aluminium is lower compared with those of steel and any ferrous alloy, a higher specific energy is required in welding due to the high reflectivity, which ranges between 0.86 and 0.90 for pure aluminium at laser wavelengths between 900 and 1,000 nm [16]. Thus, the absorption of the incident radiation is low; furthermore, the absorbed heat is rapidly transmitted to the base material due to its high thermal conductivity which is of 120 W/mK for AA 2024 and thus six times greater than that of steel.

A Trumpf TruDisk 2002 Yb:YAG disk laser was used in this work because it can increase productivity and welding quality compared to traditional rod or slab lasers. The main difference is the gain medium, which is a thin crystal disk, such that the heat dissipation occurs in the longitudinal direction rather than in the transverse direction [17, 18].

Better outputs are reached in terms of power scaling laws because multiple pump beam passes are used through the disk, and thus the demands on the power density of the pumping diodes are reduced; as a consequence, a higher total efficiency is achieved [18]. The thin disk design is therefore suitable for quasi-three-level systems such as Yb:YAG, which, in general, allows the highest energy efficiency but requires both high power densities to overcome the transparency threshold and efficient cooling at the same time [19].

Only weak thermal lensing effects arise in the disk in comparison with rod and slab lasers, thus resulting in a significant reduction in the focus diameter and an increase in the beam quality, as the divergence and the diameter variation along the propagation axis decrease [13]. In particular, a Rayleigh range of 2.8 mm is obtained with the welding system and optics in place. Consequently, a higher and nearly constant specific energy is provided through the piece thickness. A better beam quality and increased focusability allow the work piece distance to be increased, which improves the productivity in industrial contexts because it enables remote welding, which uses rapid beam deflection to eliminate non-productive idle time when moving the beam or the work piece from one welding spot to the next one [17].

When welding aluminium alloys, the advantages of the use of a disk laser allow for a better concentration of the energy to melt the base material in a keyhole shaped and fully penetrative weld; a disk laser also reduces the extent of both the fused zone and the HAZ, whose mechanical properties are lower than those in the base metal.

The work focuses on the morphological and micro-structural analysis of the welded samples to relate the welding output to the processing parameters. Energy dispersive spectrometer (EDS) analysis and Vickers micro-hardness tests were conducted. Moreover, because the ultimate tensile strength in the welded specimens is affected by the extent of the fused zone [12], an optimisation procedure for multiple response variables was performed. The optimal welding condition was finally tested via X-ray and tensile tests.

2 Design of experiments

Many variables are involved in laser welding, thus a series of structured tests must be conducted to characterise the process. Planned changes are made to the input-independent variables and the effects are assessed on the response controlled variables [20]. A proper choice of the governing variables among all of the variables involved in laser welding was based on the literature and past experience [11–13, 21]. The laser power and the welding speed are the main factors because they determine the rate of energy input to the work piece [10], and thus they definitely must be considered. The porosity is also expected to be dependent on the thermal input [21], which is the power to speed ratio.

In addition, successful laser welding requires the optimisation of other parameters, such as the size and the location of the focal spot. Indeed, to produce structurally sound and defect-free beads, welding in defocused conditions must be applied [21] by locating the beam focus point inside or outside the upper surface. Laser beams present a convergent geometry towards the waist, where the radius has a minimum; then, the beam diverges again, with a symmetrical trend. Conventionally, positive and negative defocusing designate conditions in which the focal point is placed respectively above or below the top surface of the work piece. As the specific energy provided changes, the keyhole stability is affected and the material response is different both in terms of the penetration depth and the porosity. Therefore, a change in the focus position is worth investigating.

To determine the best values for the controlling parameters to optimise the welding response, a systematic approach must be used, based both on previous studies and on ad hoc bead-on-plate (BOP) tests. Given the high reflectivity and thermal conductivity of aluminium alloys, it was found [21] that, irrespective of the welding speed, a specific power density of approximately 18.4 kW/mm^2 must be provided on the upper surface of the plates to start a keyhole mode welding on the alloy under examination. The beam geometry must therefore be considered [13] to evaluate the diameter d of the incident spot and then the specific power density P_s delivered as a function of the focus position f. The defocusing range is usually on the order of few millimetres, where the geometric features of the beam lead to a significant variation of the spot diameter anyway. Because the beam is symmetrical along the propagation axis, the same diameters for the same positive and negative defocusing values are obtained around the beam waist, where the minimum diameter is 0.300 mm for the system in place. To join 1.25 mm thick plates, 0.5 mm positive and negative defocusing was chosen to be investigated. Based on the beam geometry, a 1,344 W minimum power level must be provided to overcome the specific power density threshold value on the upper surface when defocusing the beam. A 1,400 W power level was therefore chosen as the lower limit of the power range of the experimental plan. Sensible values for welding speed were found via BOP tests while taking care to produce fully penetrative beads with no significant drop-through on the lower surface of the butting plates. Factorial experiments were then planned instead of a one-factor-at-a-time method to evaluate possible interactions between the leading independent variables.

A three-level (−1, 0, +1) experimental plan with the power, the speed, and the defocusing as governing factors was arranged; the factor levels for each parameter are listed in Table 2, where P is the power, s is the welding speed and f is the focus position.

A fractional design was preferred to reduce the amount of welds: a central composite design (CCD) was planned because it is more appropriate to create response surface models for analytical prediction. Many schemes have been suggested [20]; however, given how the region of interest relates to the operating boundaries of the experimental factors, a face-centred scheme was chosen to explore the areas within the ranges previously found via BOP tests. The tests to be performed are placed on a cubic lattice according to Fig. 1. The welding conditions are shown in Table 3, with three replications of the centre point condition as recommended in CCDs construction, while balancing the number of centre points with the number of factor involved in the analysis and aiming to achieve a relatively uniform precision inside the operating window of the processing parameters [22].

Table 2 Factor levels for input parameters

	Levels		
	−1	0	1
P (W)	1,400	1,600	1,800
s (mm/s)	50	65	80
f (mm)	−0.5	0	+0.5

Because replication aids error estimation, three runs were planned for each condition to check the dispersion in the response data and to verify the statistical significance of the measurements [22]. Then, a random test procedure was arranged both to allocate the samples and to produce the specimens, such that the observations are independent random variables to reduce experimental errors.

3 System set-up

A Trumpf BEO D70 focusing optics welding head, moved by an ABB IRB 240 M2004 robot was used to produce the samples. The system technical data are listed in Table 4. Inert gas shielding, both on the upper and lower surfaces of the plates in fully penetrative welding conditions, is required

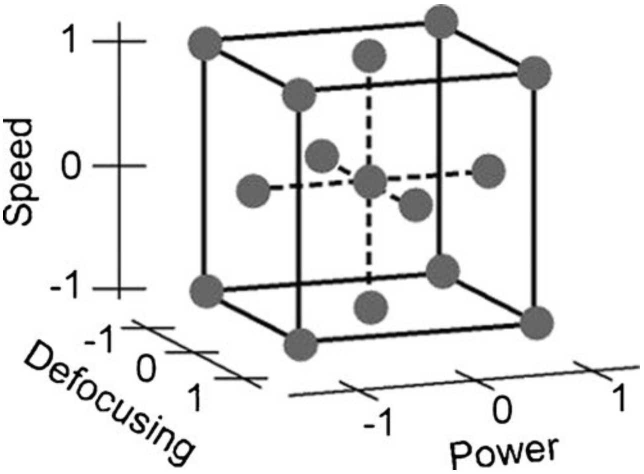

Fig. 1 Face-centred CCD

Table 3 Tests in face-centred CCD

Test	*P* (W)	*s* (mm/s)	*f* (mm)
1	1,400	50	−0.5
2	1,800	50	−0.5
3	1,400	80	−0.5
4	1,800	80	−0.5
5	1,400	50	+0.5
6	1,800	50	+0.5
7	1,400	80	+0.5
8	1,800	80	+0.5
9/10/11	1,600	65	0
12	1,600	65	+0.5
13	1,600	65	−0.5
14	1,600	80	0
15	1,600	50	0
16	1,800	65	0
17	1,400	65	0

to protect the weld pool and prevent oxidation during the process. The plume generation and, therefore, the stability of the process depend on the physical properties of the gas. Common shielding gases in aluminium welding are argon [5], helium [1, 14] and nitrogen [23]. By performing a set-up procedure, it was noticed that the argon upper shielding resulted in less absorptance due to plasma interaction; better results were achieved using helium because it has a lower ionisation energy. The results provided by Hu also indicate that helium topside shielding leads to a better process stability than argon [1]. Therefore, argon was used only for backside shielding while helium was preferred for the upper surface and was delivered via a trailing copper nozzle with a flow rate of 30 l/min opposite to the welding direction. The angle between the nozzle axis and the sheets was 25° and the flow rate, the welding direction and the nozzle angle were chosen based on the results of set-up trials. The plates were clamped on a grooved box to back shield the beads.

A high-speed compressed air cross-jet was used to protect the optics from possible molten metal spatters, which could result from fusion and are quite common when welding aluminium alloys. Additionally, a 5° sideways tilting angle was used to position the laser welding head, to prevent damage to the focusing optics and the cavity, due to the back reflection prompted by the low aluminium absorptance. The system set-up is shown in Fig. 2.

Table 4 Welding system technical data

Maximum output power (kW)	2.0
Laser light wavelength (nm)	1030
Beam parameter product (mm×mrad)	8.0
Focal length (mm)	200
Maximum power density (kW/mm^2)	28.3

4 Experimental procedure

4.1 Pre-welding operations

To conduct rigorous tests, a preliminary procedure to find the focal plane is required. Beam profilers can be adopted to conduct the test as well as Shack–Hartmann sensors, which consider wave front properties to find the beam waist section where the wave front is planar. An alternative is based on producing welding spots while moving the laser head along the beam propagation direction. An anodized aluminium sheet was used and several welding spots were made: for each spot, the distance between the laser head and the sheet was changed. Each point was spotted using a 300 W single rectangular pulse input for 50 ms, thus only producing vaporisation on the upper layer of the sheet. The spots in the resulting array were measured via optical microscopy. The same procedure was further conducted on thermal paper to fine tune the welding head position. The idea that drives the procedure is that the focus point is exactly located on the surface of the sheet when the corresponding spot has its minimum diameter. Eventually, this procedure checks the focal position to further defocus the beam.

Then, AA 2024 in 1.25 mm thick plates was considered for butt welding. The butting edges were obtained via abrasive cutting to provide homogeneous and smooth surfaces and prevent differences between specimens. Careful consideration is required in the preparation of the samples before welding because many resulting imperfections, or supposed problems, are often a direct result of improper methods to prepare the joint. Indeed, optimal welding occurs when the metal is clean and dry with a minimum oxide thickness on the surface, which may result in incomplete fusion of the base metal because the melting point of the aluminium oxide is approximately 2050 °C, which is much higher than the melting point of the base metal. Stainless steel brushes are preferred to avoid rust contamination of the joint, and a light pressure should be applied to remove the thick oxide because high forces can embed the oxide or the contaminant into the surface, thus increasing, rather than eliminating, the risk of possible weld discontinuities [4]. Any source of hydrogen, moisture or foreign material following metal working and sawing, which may dissolve in the molten metal, must also be eliminated to produce sound welds and prevent defects such as pores and inclusions [4]. Therefore, preliminary procedures are required before welding to prepare the butting edges, both within the gap and on the top and backside surfaces to a distance beyond the HAZ. A hydrofluoric and nitric acid mixture was used as a pickling

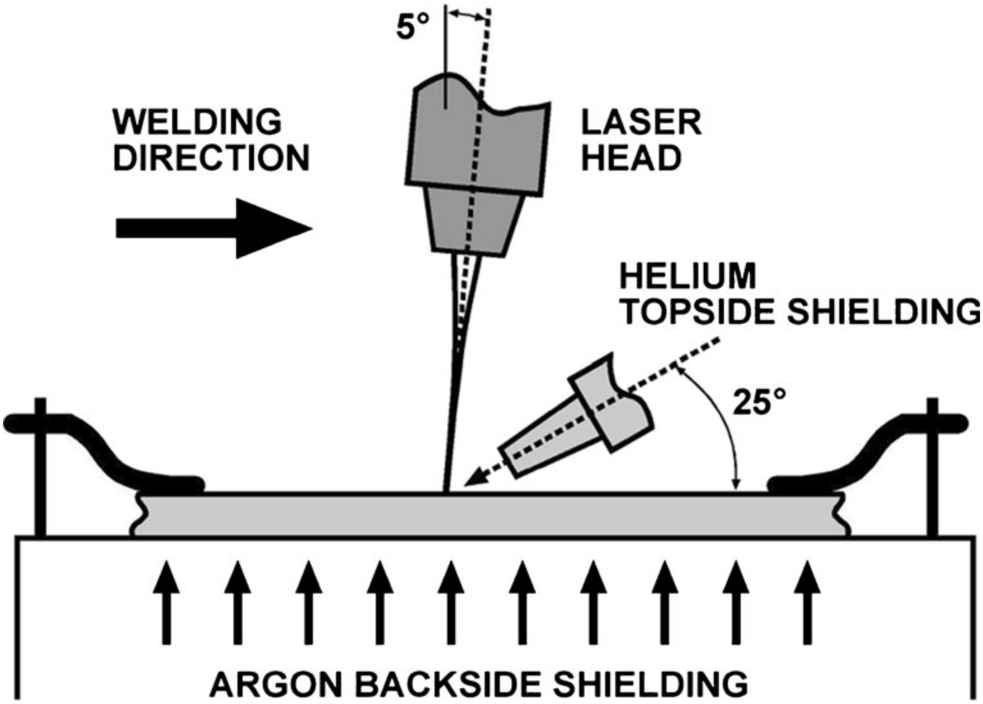

Fig. 2 System set-up

agent [4]. The aluminium plates were then further degreased with acetone immediately prior to welding.

The primary fit up is critical, given the need to minimise any gap between the plates. A system-integrated camera is employed when setting the welding path; an excellent pose and a repeatability robot accuracy of 0.03 mm can additionally maintain the alignment during the process because it has been suggested that the laser beam should not wander off the centre line by more than the 10 % of the beam diameter [10].

Before starting each test, a welding point was spotted both at the beginning and at the end of the welding path, using a 180 J single rectangular pulse input, to better tighten the samples and to prevent slippage during melting. It has been found [12] that the entry spot also plays a major role because it locally reduces the reflectivity to start a keyhole mode and enhance deep penetration. Butt autogenous weldings in continuous wave emission were then performed on 100 mm long joints.

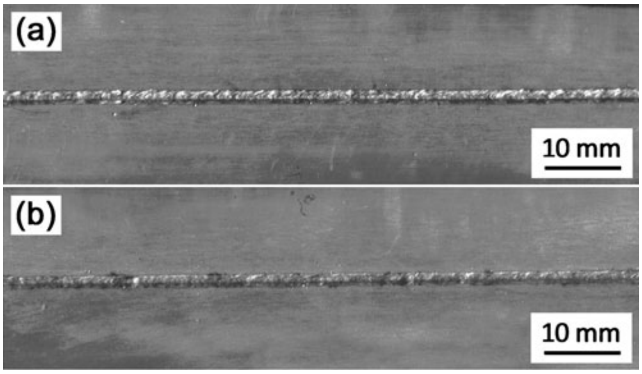

Fig. 3 Bead aspect of the sample corresponding to the CCD centre: **a** topside and **b** backside surfaces

4.2 Post-welding operations

To perform the metallographic analysis, the butt samples were cross-cut perpendicularly to the welding direction and then polished to a mirror finish with SiC paper and grinding diamond paste on polishing cloths; three cross-cuts were examined for each sample. Chemical etching was conducted using Keller’s solution at room temperature [4] to highlight the bead

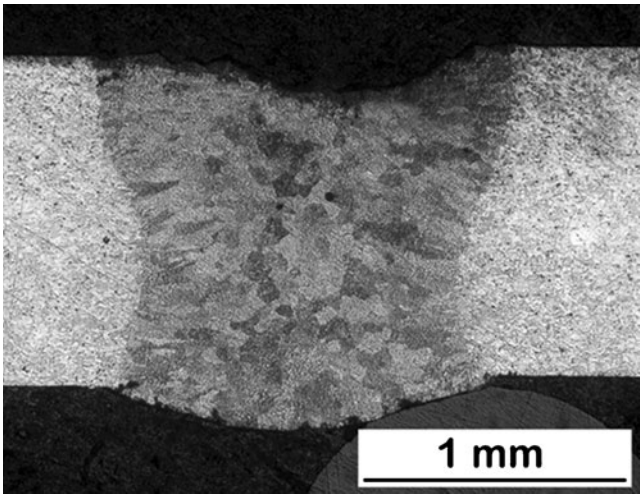

Fig. 4 Cross-section micrograph of the sample corresponding to the CCD centre

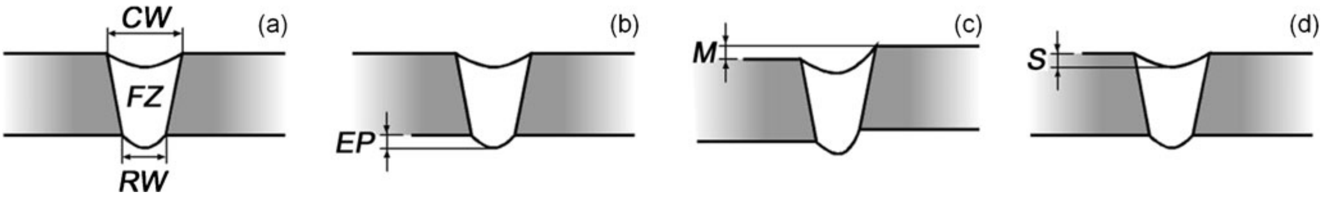

Fig. 5 Bead characterization: **a** geometric features, **b** excessive penetration, **c** misalignment, **d** sagging

boundaries in the cross-section; the etched specimens were eventually blow dried and observed using optical microscopy.

The geometric features of the cross-sections were evaluated via Nikon NIS-Elements imaging software for each operational condition by referring to international standards [24] to evaluate the welding quality level.

The concentrations of elements on transversal cross-sections were examined using a LEO EVO 50 with a LaB6 gun SEM and a resolution of 4 nm at 30 keV, equipped with an Oxford INCA Energy 300 EDS; the available EDS detector can provide information starting from elements with atomic number higher than 4. Analyses were performed with a 20 keV primary energy with a probe current of 100 pA. The Vickers micro-hardness was tested on cross-sections according to the referred specification [25] using a LeicaVM HTAuto. A 0.981 N (i.e. 0.1 kgf) load was used for 15 s ata speed of 60 μm/s. Micro-hardness tests were performed 1 week after welding to allow the stabilisation of material properties during its average period of natural ageing [2, 4]. Eventually, to further characterise the samples, X-ray tests were conducted with a General Electric CRx Flex CR Scanner and an MTS Insight 30 was used for tensile tests.

5 Results and discussion

First, visual inspections were performed on both sides: the bead width on the upper crown was found to be constant along the welding line and no oxidation was detected on the upper surface or on the backside. No significant distortions in the plates were produced. As an example, the top and backside surfaces of the sample corresponding to the CCD centre are shown in Fig. 3; the micrograph is shown in Fig. 4.

Then, the geometric features and the common imperfections were evaluated according to the reference guidance for electron and laser beam welding [24]. The crown width, the root width and the fused zone extent were considered to describe the welding bead geometry. Three types of common imperfections in aluminium alloys require special considerations for the specimens under examination: the excessive penetration (EP) on the backside surface, the misalignment (*M*) between the butting edges and the incompletely filled groove with sagging (*S*) on the top surface (Fig. 5).

The average values of geometric features and imperfections due to the three cross-sections of each three-time-repeated sample are listed in Table 5, where conditions 9, 10, and 11 are merged, because they are referred to the same processing parameters of the CCD centre point. Because the standard deviations have been found to be considerably low for each measure under any operating conditions, the data points tend to be close to the mean and therefore are worth considering in further analyses.

According to the specification, because the thickness is 1.25 mm, the stringent quality category, which is the best category possible, is met for EP and *M* because their values have been found to be lower than 0.39 and 0.13 mm, respectively. Misalignment was discussed also, although one should assume that it is affected by the improper clamping of the plates rather than by the processing parameters.

The reference quality level values for *S* must be evaluated for each operating condition which are not only dependent on the plate thickness, but also on EP because the specification allows a tradeoff between sagging and excessive penetration, provided some specific conditions on the sheet

Table 5 Values of geometric features and imperfections for the different welding conditions

Test	CW (mm)	RW (mm)	FZ (mm^2)	EP (mm)	*M* (mm)	*S* (mm)
1	1.80	1.36	1.93	0.10	0.06	0.07
2	1.53	1.03	1.54	0.04	0.06	0.06
3	1.37	0.84	1.33	0.07	0.02	0.00
4	1.40	1.15	1.49	0.13	0.01	0.08
5	2.03	1.41	2.24	0.10	0.02	0.10
6	1.84	2.04	2.38	0.14	0.01	0.18
7	1.51	0.90	1.40	0.01	0.02	0.04
8	1.57	1.26	1.67	0.16	0.01	0.11
9/10/11	1.59	1.34	1.71	0.11	0.02	0.09
12	1.76	1.37	1.87	0.11	0.04	0.10
13	1.54	1.30	1.62	0.09	0.02	0.06
14	1.50	1.14	1.57	0.14	0.03	0.01
15	1.78	1.63	2.00	0.17	0.01	0.22
16	1.51	1.40	1.65	0.10	0.01	0.18
17	1.57	1.31	1.66	0.13	0.02	0.09

CW crown width, *RW* root width, *FZ* fused zone extent, *EP* excessive penetration thickness and the crown width [24]. Therefore, stringent quality levels are met when the following condition applies:

$$S \leq 0.1 \cdot t + \mathrm{EP}$$

where t is the sheet thickness. The stringent quality requirements were effectively matched. It must be stressed that because the mere average values in the case of defects may lead to misjudgments, each cross-section from each replication was considered separately to assess the joint quality. It is generally expected that one quality level can cover the dimensional limits for any possible imperfections in the same joint; nevertheless, it must also be noted that, for certain applications for aluminium alloys, such as in fatigue loading or leak tightness, the standard allows to definition of different quality levels for imperfections in the same welded joint, such that the overall quality level can be defined by the application standard on a case-by-case basis in conjunction with the concerned parties [24].

Other defects, such as undercuts or shrinkage grooves which are described in the specification, were occasionally produced in the experimental plan; nevertheless, the defects met the quality levels as well. According to the micrographs of the samples, no boundaries of the HAZ are detected, so additional exams via micro-hardness tests were conducted to assess its extent and are discussed in the following.

5.1 Porosity

Porosity development is one of the main issues in the laser welding of aluminium alloys, and thus it must be taken into account when searching for an optimal welding strategy. Two types of porosity may arise [13, 15, 26]: the micro- and macro-porosity, which differ in terms of their pore diameter ranges and their formation process. Because macro-pores are distributed along the welding bead centre line [21, 26], measurements of their content and extent should be conducted on longitudinal sections of the bead instead of the cross-sections, for a more reliable calculation. Because the width of welded samples obtained in this analysis is very narrow, a proper cut for the observation of the porosity is not feasible. Nevertheless, it is possible to infer hypotheses even from qualitative inspections of the cross-sections already produced for geometric characterization. Indeed, previous studies [13, 21] on the welding of 3.2 mm thick plates of the same alloy, whose beads were larger due to the higher specific energy required, have shown that any significant content of macro-pores is detected statistically even in cross-sections. Because none of the cross-sections of the samples analysed in this study showed macro-porosity, at this stage of the analysis, one could assume that the parameter window under examination does not affect the keyhole stability significantly, which is considered to be the main reason for macro-porosity formation [1], although this issue will be further addressed in the following sections. However, isolated evidence of micro-porosity, which normally does not result in the rejection of welded parts [24], was detected in the cross-sections and is ascribed to hydrogen and other common gases, which are released and trapped in the solidifying alloy because their solubility in liquid metal is much higher compared to their solubility in the solid state [4, 15]. Although the quality requirements are met, specimens differ in terms of micro-porosity. In particular, a higher amount of micro-pores was

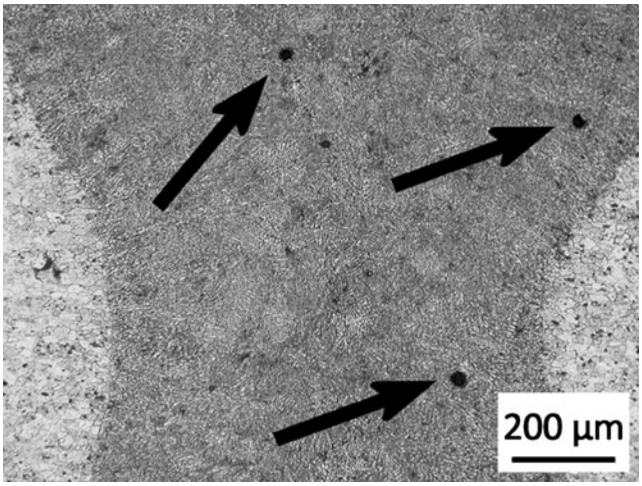

Fig. 6 Micro-pores distribution in the specimen obtained with 1.6 kW power level, 80 mm/s speed, focused conditions

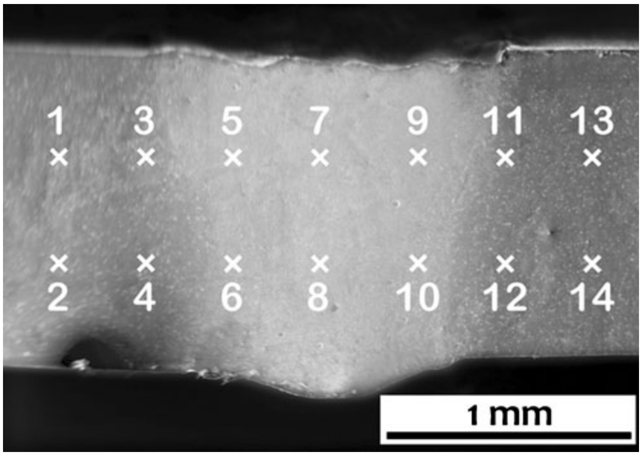

Fig. 7 Scanning strategy for EDS analysis

Table 6 Magnesium content percentage in the scanned EDS pattern

Spot 1	Spot 3	Spot 5	Spot 7	Spot 9	Spot 11	Spot 13
1.48	1.35	1.16	1.18	1.15	1.45	1.40
Spot 2	Spot 4	Spot 6	Spot 8	Spot 10	Spot 12	Spot 14
1.34	1.47	1.03	1.14	0.99	1.55	1.47

detected for the specimen in condition 14, whose micrograph is shown in Fig. 6.

Because the porosity is expected to be dependent on the power to speed ratio, which is normally referred to as the thermal input [21], a comparison between the specimen in condition 14 and the specimen in condition 15 was conducted, where the latter experienced a higher thermal input as a consequence of the same power at a lower speed in the same focusing condition. No significant micro-porosity was found for the specimen in condition 15. Further analyses of the concentrations of elements were then conducted. Because previous studies on 3.2-mm thick plates have shown that the porosity development is related to magnesium vaporisation in the fused zone due to the welding thermal cycle, significant porosity is produced when higher magnesium percentages are lost [13]. The samples in conditions 14 and 15 were subjected to EDS inspections: a decrease in magnesium content, from 1.44 % in the base material to an average of 1.10 % in the fused zone, was observed in sample in condition 14 while no significant reduction was detected in the sample in condition 15. A map for the scanning strategy is shown in Fig. 7, which refers to the specimen in condition 14. The corresponding magnesium percentages for each point are listed in Table 6. The micro-porosity formation therefore appears to follow the same behaviour observed for the macro-porosity on thicker plates depending on magnesium content [21]; nevertheless, the reasons are different because the thermal inputs in the welding of thinner plates are 1 order of magnitude lower. It is inferred that the operative conditions in which hydrogen acts as a micro-porosity starter also produce a magnesium migration towards the cavities, and thus a reduction in magnesium content is observed via EDS when considering the fused zone.

Based on the EDS analysis, additional comments can be provided. Because the speeds adopted are higher than the speeds that are normally used to weld samples with greater thickness [12, 13], the vaporisation of the alloying elements is lower as a consequence of the shorter interaction period between the material and the heat source imposed by the laser beam. Samples of 3.2 mm were welded using a speed of 10 mm/s: an average loss of magnesium in the order of 53 % was estimated. Moreover, as already noted before, the lower magnesium vaporisation also affects the macro-porosity because it changes the balance of the keyhole pressure towards a condition of stability.

5.2 Softening in the fused zone

Vickers micro-hardness measurements were conducted on the welding beads in order to characterise the weld-affected area. Because the beads were performed in fully penetrative conditions, indentations were made at the mean height with respect to the thickness, so at a height of 0.625 mm from the top surface of the plate.

The mechanical properties in aluminium alloys do not depend only on the alloying elements but also on the heat treatment [4]. AA 2024 in the T3 state is considered in this study; this designation applies to cold-worked products whose strength has been improved after solution heat treatment. The mechanical properties are then stabilised by room temperature ageing. The enhanced strength in the base alloy is due to magnesium addition and finely dispersed

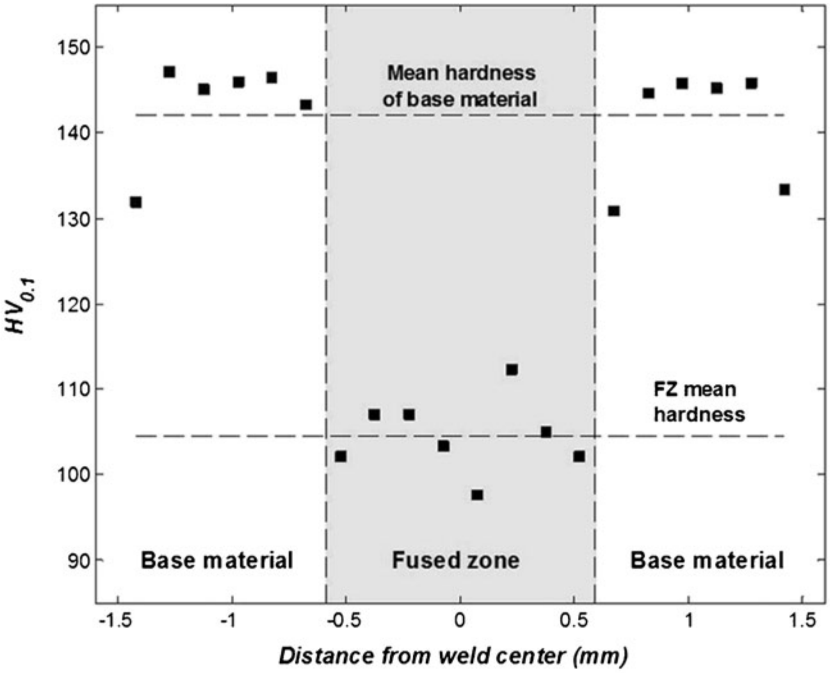

Fig. 8 Micro-hardness results for the specimen obtained with 1.4 kW power, 80 mm/s speed and 0.5 mm positive defocusing

precipitates following ageing heat treatments. In particular, as little as approximately 0.5 % Mg is effective in changing the ageing characteristics of the alloy [4].

Degradation and material softening both in the bead and in the HAZ are caused by a phase transformation because the dissolution of precipitates occurs due to the high temperatures experienced in the areas during welding thermal cycles [4, 10]. Micro-segregation occurs during solidification [1], and no allotropic modifications occur [2].

A preliminary evaluation of the mechanical properties is feasible via micro-hardness testing. A decrease, as expected for any precipitate strengthened aluminium alloy, is observed in the weld fusion zone compared to the base metal, which is consistent with other results in literature [1, 3]. No significant difference in the values and the trend were found for the tested specimens, irrespective of the processing parameters. The micro-hardness ranged between 135 and 145 $HV_{0.1}$ in the base material, as expected according to material data sheets [4], and between 105 and 110 $HV_{0.1}$ in the fused zone. No transition values were observed between the zones, and thus it is not possible to assess the extent of the HAZ, which is assumed to be less than the distance between two consecutive indentations, i.e. 150 μm according to the referred specification [25]. Larger HAZs are a result of different laser sources when welding the same alloy [1, 3]. As an example, the results for the specimen obtained with a power of 1.4 kW, a speed of 80 mm/s and a positive defocusing of 0.5 mm are shown in Fig. 8.

6 Modelling and optimisation

Once it is proved that the welds meet the quality requirements for each possible imperfection, the response variables to optimise the process must be defined. The extent of the fused zone was considered because its mechanical features are lower compared to the base material and therefore they affect the bead ultimate tensile strength [12]. Furthermore, an appropriate shape factor of the bead was defined. As observed in the cross-sections, no necking zones were observed in the bead while they are common when welding other materials. It is possible, therefore, to refer to a shape factor that only considers the root to crown ratio, irrespective of the bead profile at the mean height.

Some preliminary conclusions were drawn from the main effects plots. The expected basic relationships were confirmed: any increase in the laser power yields a proportional increase in the response variables. Similarly, any increase in the welding speed results in a

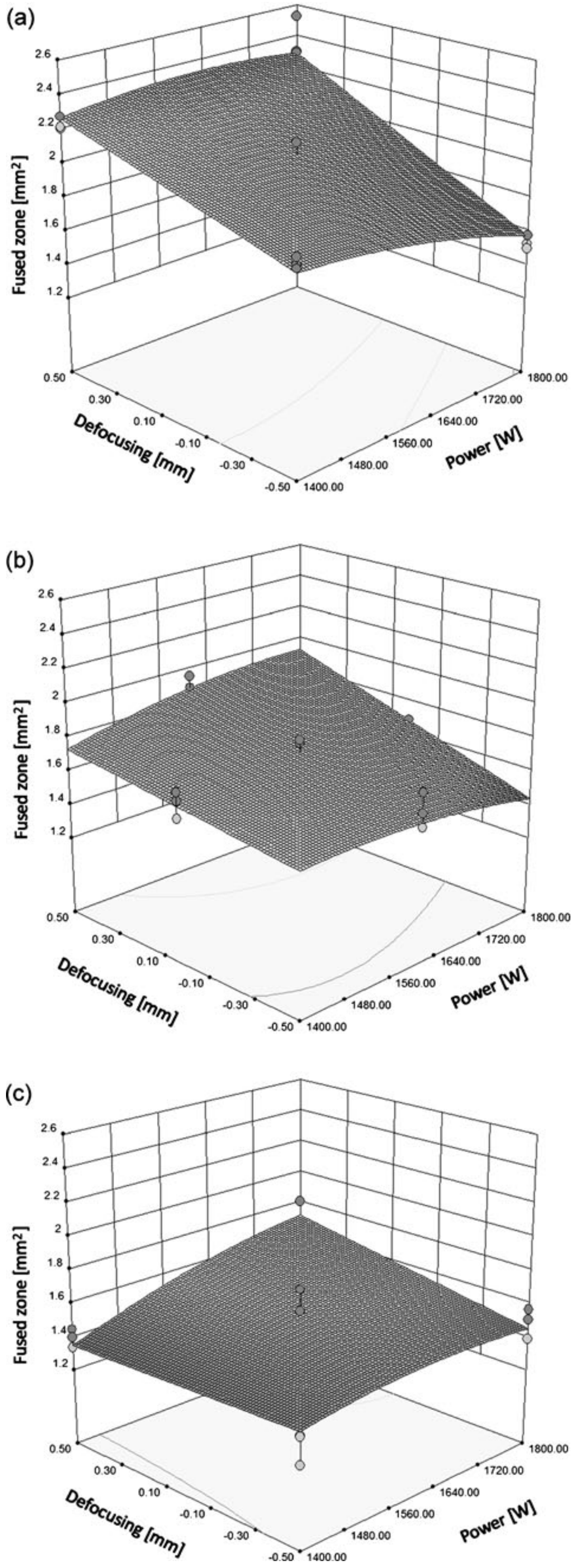

Fig. 9 Response surfaces for the fused zone with **a** 50 mm/s, **b** 65 mm/s and **c** 80 mm/s welding speed

Table 7 Processing conditions with corresponding response variables and desirability values as suggested in the optimization process

	P (W)	*s* (mm/s)	*f* (mm)	FZ (mm^2)	SF	Desirability
1	1,400	80	0.50	1.35	0.54	0.901
2	1,400	80	0.49	1.35	0.55	0.900
3	1,400	80	0.48	1.35	0.56	0.900
4	1,400	80	0.45	1.35	0.57	0.899
5	1,400	80	0.44	1.35	0.57	0.898

FZ fused zone extent, *SF* shape factor

corresponding decrease in the referred variable. On the other hand, the effect of the focus position seems not be decisive, although an increase in the fused zone is achieved with positive defocusing.

The models for both the fused zone and the shape factor were produced with quadratic interactions among the governing factors; the corresponding *p* values were considered as indicators of significance [22]. *P* values of 0.0341 and less than 0.0001 were achieved, respectively. As an example, to show the effects of the processing factors, the response surfaces for the fused zone for each level of the welding speed are shown in Fig. 9a–c. Interestingly, it is clear from their shape and already confirmed in the estimation coefficient of the model in the ANOVA analysis, that the actual effect of the power is quite moderate compared to the effects of the speed and the defocusing, which affect the predicted value significantly. A similar behaviour is noticed when examining the shape factor.

The next logical step is the optimisation of the referring response variable, and thus specific criteria must be defined. In principle, the minimisation of the fused zone is required. Additional constraints must be added to involve the shape factor. Given the fact that all of the beads have the typical keyhole shape, with the boundary narrowing towards the root, the beads whose root width is close to the crown have to be rejected because this condition is indicative of welding conditions between the conduction and the keyhole regimes. In addition, the beads whose root is too narrow must be rejected because it has been shown that this condition would hamper the expulsion of vapour, resulting in porosity [12]. Based on these considerations, an optimal range between 0.5 and 0.7 was chosen for the shape factor. Under this constraint, the fused zone optimisation procedure was conducted.

Many procedures are feasible for solving constrained nonlinear optimization problems, such as successive linear programming, successive quadratic programming, the penalty and barrier function methods, and augmented Lagrangian functions. The penalty function method was preferred in this work to convert the constrained optimisation problem into an unconstrained one. The idea is to modify the original model by the addition of constraints in such a manner as to have the optimum be found and the constraints be satisfied. The constraints were added to the optimisation model in such a way as to penalise the conditions that do not approach the optimum of the model or satisfy the constraint equations.

The original nonlinear model used in this work is the fitted regression equation. The goals are combined into an overall desirability function. This approach is one of the most widely used in industry for the optimizsation of multiple response processes and it is based on the idea that a product or a process that has multiple quality characteristics is completely unacceptable if even only one of them drops outside of some desired limits. The method finds the operating conditions that provide the most desirable response values. For each response Y_i (x), the desirability function d_i (Y_i) assigns numbers ranging between 0 and 1 to the possible values of Y_i, with d_i (Y_i)=0 representing a completely undesirable value of Y_i and d_i (Y_i)=1 representing a completely desirable or ideal response value. The individual desirability values are then combined using a geometric mean, which gives the overall desirability D:

$$D = [d_1(Y_1) \cdot d_2(Y_2) \cdot \ldots \cdot d_k(Y_k)]^{\frac{1}{k}}$$

with k denoting the number of responses. Depending on whether a particular response Y_i is to be maximised, minimised, or targeted, different desirability functions d_i (Y_i) can be used. A useful class of desirability functions was proposed by Derringer and Suich [27]. The first five solutions of the optimisation process are listed in Table 7 with their corresponding desirability values.

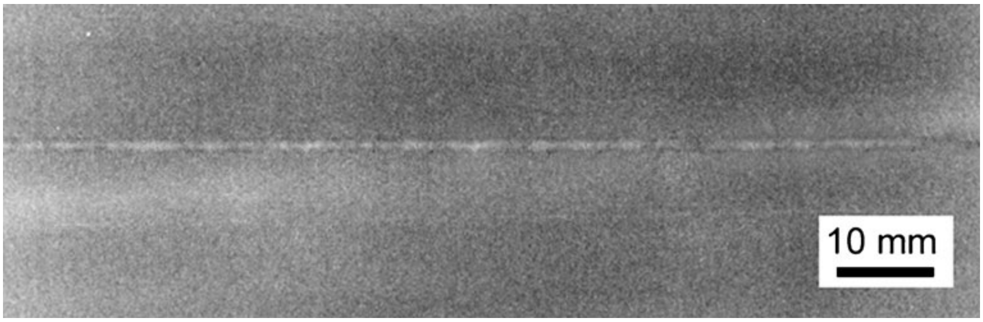

Fig. 10 X-ray transmitted image of the welding bead in condition 7

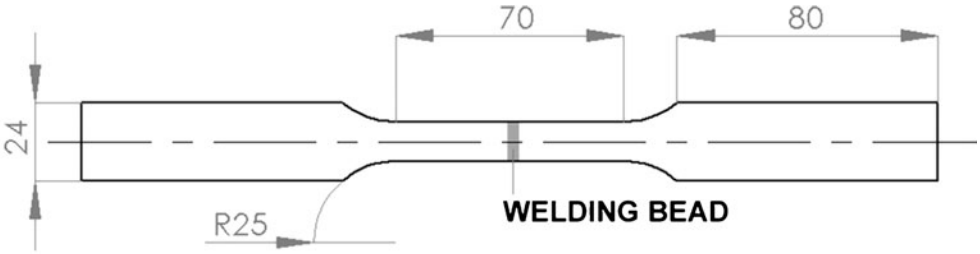

Fig. 11 Dimensions of the tensile test specimen

An optimal welding condition whose corresponding processing parameters are a power of 1.4 kW, a speed of 80 mm/s and a positive defocusing of 0.5 mm is suggested because it has the highest desirability function value and is very robust without any significant variation in the response variables and the desirability output even when affected by minor changes in the defocusing value within the Rayleigh range. The condition was actually tested in the experimental plan as condition number 7 (Table 3); its micro-hardness trend along the bead is shown in Fig. 8.

7 Analysis of the optimal condition

The final analyses to characterise the bead in terms of the porosity and the tensile strength, were conducted for the optimal welding conditions. The cross-section was already considered at a previous stage of the analysis and the micro-porosity was found to be low. Although the macro-porosity is also expected to be low given the cross-sectional appearance when cutting the specimens along the transverse direction, further tests are now required to verify the assumption for the suggested processing conditions. Three 100 mm long beads were produced and then tested; the resulting X-ray transmitted image is shown in Fig. 10.

No cracks or macro-pores were detected, and thus the joints can be considered defect-free. Nevertheless, given that a decrease in the micro-hardness was observed in the bead compared to the standard values in the base material, tensile tests are required to assess the joint quality in terms of the mechanical features. Given the micro-hardness trend in the cross-section, the fracture is expected to increase into the welding bead, as already proved with the same alloy for sheets of a different thickness [12]. It has also been observed that the failure mode with aluminium alloys depends on the alloy type and on the heat treatment and the welding conditions, which affect the extent of the fused zone [3, 12]. The specimen for the tensile test was designed in accordance with UNI EN ISO 4136:2011 [28] and is shown in Fig. 11.

Table 8 UTS values for specimens in condition 7

Test	UTS (MPa)	UTS/UTS$_0$ (%)	Elongation (%)
1	385	80	1
2	369	77	1
3	357	74	1

A non-welded sample was tested: its ultimate tensile strength (UTS)$_0$ was found to be 480 MPa and its percent elongation at break was 18 %, as expected from the material data sheets [4]. Three specimens were then milled from three independent welding beads and then tested at a cross-head speed of 0.015 mm/s after they were loaded in the direction perpendicular to the welding bead. It is widely accepted in several studies on different aluminium alloys [3, 29–31] that any welding bead showing a UTS higher than 66 % of the base material is acceptable. The percent elongation at break and the UTS resulting from the tensile tests are listed in Table 8. The UTSs are also compared to the value obtained with the original and non-welded sample.

An average value of 370 MPa, which is 77 % of the UTS of the base material, was the result, and thus an improvement is evident because lower values, below 69 %, were achieved with a Nd:YAG source on a 0.8 mm thick sheet. A similar value is expected with a CO$_2$ source [3].

The cracks in each tested specimen start from the weld and grow towards the interface between the weld and the base material, where a steep discontinuity is experienced in crossing zones with different mechanical features, as shown in the micro-hardness analysis. The top- and back-side crack surfaces are shown in Fig. 12. The results of the X-ray and tensile tests are satisfactory and therefore support the choice of the optimal condition previously suggested through the optimisation process.

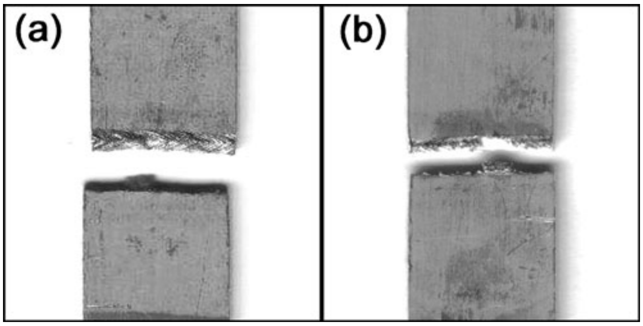

Fig. 12 Top- (**a**) and back-side (**b**) crack surfaces for a welded specimen in the optimal processing condition

8 Conclusions

Using a disk laser source and an adequate parameter window based on previous experience and ad hoc bead-on-plate tests, narrow beads with no significant defects were obtained by joining 1.25 mm thick AA 2024 sheets, which met the reference international standards in terms of excessive penetration, sagging on the top surface and misalignment. A qualitative analysis was conducted on the content of the pores: no macro-porosity affects the joint. The micropores were observed in certain welding conditions and are thought to be related to thermal inputs and magnesium vaporiation according to the energy dispersive spectrometer results. Higher welding speeds compared to the speeds used to weld thicker plates can reduce the magnesium loss in the fused zone.

The Vickers micro-hardness tests showed a decrease in the hardness of the bead compared to the base metal, due to the thermal cycles experienced during welding, which results in the dissolution of precipitates and phase transformation. However, no difference in the micro-hardness values and the trend in the bead were found, irrespective of the processing parameters. The resulting heat-affected zone extent is deemed to be narrower than 150 μm.

An optimisation procedure was developed to assess an optimal set of parameters, considering fused zone and a shape factor as reference variables. The values of the corresponding desirability function suggest an optimal welding condition with a power of 1.4 kW, a speed of 80 mm/s and 0.5 mm of positive defocusing, which, according to the micrograph analysis, also results in no microporosity. X-ray and tensile tests were performed to assess the mechanical quality of the suggested welding condition: no macro-pores were detected, and the ultimate tensile strength was determined to be over the accepted threshold value for the alloy under examination because 370 MPa are obtained on average, with a significant improvement compared with the results obtained with other laser sources.

Acknowledgments The authors acknowledge Dr. Antonio Vecchione and Dr. Rosalba Tatiana Fittipaldi of CNR-SPIN U.O.S. Salerno and Dipartimento di Fisica “E.R. Caianiello” Università di Salerno for EDS inspections; Dr. Michele Di Foggia of Europea Microfusioni Aerospaziali S.p.A. for X-ray tests; and Prof. Gabriele Cricrì, Dr. Michele Perrella and Dr. Marcello Lepore of Dipartimento di Ingegneria Industriale Università di Salerno for tensile tests.

References

1. Hu M, Richardson IM (2005) Autogenous laser keyhole welding of aluminium alloy 2024. J Laser Appl 17(2):70–80
2. Gulyaev A (1980) Light metals and alloys. In: Physical metallurgy 2. Mir, Moscow, pp 234–269
3. Ludovico AD, Daurelio G, De Filippis LAC, Scialpi A, Squeo F (2005) Laser welding of the AA 2024-T3 aluminium alloy by using two different laser sources. Proc SPIE 5777:887–894
4. ASM International (1993) Aluminum and aluminum alloys. Davis, USA
5. Malek Ghaini F, Sheikhi M, Torkamany MJ, Sabbaghzadeh J (2009) The relation between solidification and liquation cracks in pulsed laser welding of 2024 aluminum alloy. Mater Sci Eng, A 519:167–171
6. Aydin H, Bayram A, Uguz A, Akay KS (2009) Tensile properties of friction stir welded joints of 2024 aluminum alloys in different heat-treated-state. Mater Des 30:2211–2221
7. Preston RV, Shercliff HR, Withers PJ, Smith S (2004) Physically-based constitutive modelling of residual stress development in welding of aluminium alloy 2024. Acta Mater 52:4973–4983
8. Kalita SJ (2011) Microstructure and corrosion properties of diode laser melted friction stir weld of aluminum alloy 2024 T351. Appl Surf Sci 257(9):3985–3997
9. Capello E (2008) Le lavorazioni industriali mediante laser di potenza. Maggioli Editore, Bologna
10. Duley WW (1998) Laser welding. Wiley, New York
11. Steen WM (2003) Laser material processing. Springer, London
12. Cardaropoli F, Alfieri V, Caiazzo F, Sergi V, Campanile G (2011) Laser welding of aluminum alloy AA 2024 by Yb-YAG disk laser. Proc. X AITeM Conference, Enhancing the Science of Manufacturing 1–16
13. Alfieri V, Cardaropoli F, Caiazzo F, Sergi V (2011) Porosity evolution in aluminum alloy 2024 BOP and butt defocused welding by Yb:YAG disk laser. Eng Rev 31(2):125–132
14. Kim JK, Lim HS, Cho JH, Kim CH (2008) Weldability during the laser lap welding of Al 5052 sheets. Arch Mater Sci Eng 31 (2):113–116
15. Haboudou A, Peyre P, Vannes AB, Peix G (2003) Reduction of porosity content generated during Nd:YAG laser welding of A356 and AA5083 aluminum alloys. Mater Sci Eng, A 363:40–52
16. Bartl J, Baranek M (2004) Emissivity of aluminium and its importance for radiometric measurement. Meas Phys Quant 4 (3):31–36
17. Giesen A, Speiser J (2007) Fifteen years of work on thin-disk lasers: results and scaling laws. IEEE J Sel Top Quantum Electron 13(3):598–609
18. Kemp AJ, Valentine GJ, Burns D (2004) Progress towards high-power, high-brightness neodymium-based thin-disk lasers. Progr Quantum Electron 28:305–344
19. Javadi-Dashcasan M, Hajiesmaeilbaigi F, Razzaghi H, Mahdizadeh M, Moghadam M (2008) Optimizing the Yb:YAG thin disc laser design parameters. Opt Commun 281:4753–4757
20. Montgomery DC (2005) Design and analysis of experiments. Mc-Graw Hill, New York
21. Alfieri V, Cardaropoli F, Caiazzo F, Sergi V (2012) Investigation on porosity content in 2024 aluminum alloy welding by Yb:YAG disk laser. Adv Mater Res 383–390:6265–6269
22. Anderson MJ, Whitcomb PJ (2007) DOE simplified. Productivity Press, Portland
23. Sanchez-Amaya JM, Delgado T, Gonzalez-Rovira L, Botana FJ (2009) Laser welding of aluminium alloys 5083 and 6082 under conduction regime. Appl Surf Sci 255(23):9512–9521
24. EN ISO 13919–2 (2003) Welding—electron and laser beam welded joints—guidance on quality levels for imperfections—Part 2: Aluminum and its weldable alloys
25. EN ISO 6507–1 (2005) Metallic materials—Vickers hardness test —part 1: test method
26. Pastor M, Zhao H, Martukanitz RP, Debroy T (1999) Porosity, underfill and magnesium loss during continuous wave Nd:YAG laser welding of thin plates of aluminum alloys 5182 and 5754. Weld J 78(12):207–216

27. Derringer G, Suich R (1980) Simultaneous optimization of several response variables. J Qual Technol 12(4):214–219
28. UNI EN ISO 4136 (2011) Destructive tests on welds in metallic materials—transverse ensile test
29. Chao YJ, Qi X, Tang W (2003) Heat transfer in friction stir welding—experimental and numerical studies. J Manuf Sci Eng 125:138–145
30. Chang WS, Rajesh SR, Chun CK, Kim HJ (2011) Microstructure and mechanical properties of hybrid laser-friction stir welding between AA6061-T6 Al alloy and AZ31 Mg alloy. J Mater Sci Technol 27 (3):199–204
31. Scialpi A, De Filippis LAC, Cavaliere P (2007) Influence of shoulder geometry on microstructure and mechanical properties of friction stir welded 6082 aluminium alloy. Mater Des 28(4):1124–1129